Regional simulations of deep convection and biomass burning over South America:
1. Model evaluations using multiple satellite data sets

Longtao Wu,[1] Hui Su,[1] and Jonathan H. Jiang[1]

[1] Multiple data sets, mostly from satellite observations, are used to evaluate the performance of the Weather Research and Forecasting model with Chemistry (WRF-Chem) in simulating the distribution and evolution of aerosol, clouds, precipitation and chemistry during the dry season in South America. A 9-day WRF-Chem simulation with 36 km horizontal resolution is performed from 15 to 24 September 2006, during which frequent biomass burnings were observed. It is shown that the model reproduces the spatial distribution of aerosols produced by biomass burning and approximately captures convective transport of trace gases (e.g., CO and O_3) into the upper troposphere. Surface precipitation is also in reasonable agreement with observation. The model simulations overestimate the magnitude of water vapor in the upper troposphere while the magnitude of cloud water content is lower than measurements from satellites, which may indicate problems in the cumulus and microphysical parameterizations. The model simulations capture temporal variations of outgoing longwave radiation at the top of atmosphere and downward shortwave radiation at the surface shown in the NASA GEWEX SRB data set. A sensitivity run at 4 km horizontal resolution shows similar results to the 36 km simulation, with a high bias of precipitation. The uncertainty and weakness in both satellite observations and model simulations are identified. This study demonstrates that satellite data are valuable to the evaluation of regional model simulations for climatologically important processes such as deep convection and biomass burning, especially in regions with little in situ observation.

Citation: Wu, L., H. Su, and J. H. Jiang (2011), Regional simulations of deep convection and biomass burning over South America: 1. Model evaluations using multiple satellite data sets, *J. Geophys. Res.*, *116*, D17208, doi:10.1029/2011JD016105.

1. Introduction

[2] Biomass burning events coupled with deep convection inject a large amount of aerosols and trace gases into the atmosphere, which can affect both climate and air quality. Observational studies [e.g., *Andreae et al.*, 2001; *Folkins et al.*, 1997] have shown that deep convection significantly enhanced the upper tropospheric carbon monoxide (CO) and ozone (O_3) by transporting biomass burning emissions to upper troposphere. Extensive studies through field experiments and satellite observations have been conducted to understand the impact of biomass burning aerosols on both global and regional climate. *Andreae et al.* [2004] found delayed precipitation and reduced cloud droplet size associated with biomass burning pollution. Suppressed precipitation and reduce ice particle effective radius were also found in polluted clouds over South America, compared to the clean clouds with the similar ice water content (IWC) [*Jiang et al.*,

2008]. In contrast, *Lin et al.* [2006] showed that enhanced aerosols in the Amazon were associated with increased precipitation, increased cloud cover and decreased cloud top temperature/pressure in 2002 and 2004.

[3] There have been a number of model simulations on the aerosol effects on the regional weather and climate [e.g., *Martins et al.*, 2009; *Zhang et al.*, 2008, 2009]. However, the modeling studies with simultaneously varying thermo-dynamic conditions and aerosol concentrations are rather limited. It has been shown that a fully coupled meteorology-chemistry-aerosol model can capture regional cloud variations better than uncoupled models [*Gustafson et al.*, 2007].

[4] The Weather Research and Forecasting model (WRF) is a state-of-the-art mesoscale weather prediction system. The chemistry version of the WRF model (known as WRF-Chem) [*Grell et al.*, 2005] is one of the representative models with fully coupled meteorology, chemistry and aerosol. The WRF-Chem model has been widely used to study the inter-actions among aerosols, chemical tracers and meteorological conditions [e.g., *Chapman et al.*, 2009; *Gustafson et al.*, 2007; *Ntelekos et al.*, 2009; *Tie et al.*, 2009; *Lin et al.*, 2010; *Zhao et al.*, 2010]. The WRF-Chem working group has continued working on improvement of the model system. Some validations of the model performance have been done

[1]Aura Microwave Limb Sounder (MLS) Science Team, Jet Propulsion Laboratory, California Institute of Technology, Pasadena, California, USA.

recently [e.g., *Chapman et al.*, 2009; *Fast et al.*, 2009; *Tie et al.*, 2009; *Barnard et al.*, 2010; *Lin et al.*, 2010; *Zhao et al.*, 2010]. *Chapman et al.* [2009] evaluated the WRF-Chem simulations over northeastern North America during the summer of 2004 with a few independent atmospheric field measurements. With the measurements from the 2006 Megacity Initiative: Local and Global Research Observations (MILAGRO) field campaigns, *Fast et al.* [2009], *Tie et al.* [2009] and *Barnard et al.* [2010] evaluated the WRF-Chem simulated aerosols and trace gases in the vicinity of Mexico City. The simulated concentrations of CO, ethane, O_3 and peroxyacetyl nitrate (PAN) over East Asia were evaluated with the TRACE-P (Transport and Chemical Evolution over Pacific) field campaign in March 2001 [*Lin et al.*, 2010]. *Zhao et al.* [2010] used both surface and satellite observed aerosol optical thickness (AOT) to evaluate the model simulations of dust aerosols. Most of the validations were based on field campaigns or surface observations, which were limited to point sources of data or a short duration.

[5] Multiple satellite observations provide valuable sources to evaluate the performance of model simulations, especially in regions that are lack of in situ measurements. In particular, the A-Train constellation provides a suite of satellite measurements from space for atmospheric thermodynamic conditions (temperature and humidity), clouds, aerosols and chemical composition [*L'Ecuyer and Jiang*, 2010]. These satellite observations have been underutilized for regional model simulations for a number of reasons. First, the unique sampling frequency and spatial coverage of satellite measurements are not directly comparable to gridded outputs from models. For example, the CloudSat radar measurements and the lidar measurements from the Cloud-Aerosol Lidar and Infrared Pathfinder Satellite Observations (CALIPSO) are narrow slices of cloud and aerosol profiles at two local times per day. It needs to be investigated how to compare the limited samples from these satellite observations with regional model simulations. Second, observed vertical profiles from satellites are usually associated with "averaging kernels," which represent the vertical weighting functions of each vertical level to the total radiance measured by the satellite instruments. Thus, a fair comparison of satellite data with model simulations needs to take into account the "averaging kernels" effect. Third, satellite retrievals carry uncertainties. It is important to know the uncertainties of data when comparing to the model results. Nevertheless, the wealth of satellite data should be fully explored. Moreover, multiple independent satellite measurements provide complementary information on chemical and dynamical processes. Synergistic combination of these data offers multiangle insights into particular processes and facilitates understanding the physics of these processes. For example, accurate simulation of deep convection has been notoriously difficult for models. Conventionally, only precipitation and cloud profiles are used for diagnosis of convective activity. However, chemical tracers, such as CO and O_3, bear useful information for convective mass transport and thus can be used to test convective parameterizations in models [*Liu et al.*, 2010; *Hegarty et al.*, 2010]. Similarly, AOT can be simulated in models approximately correct but for wrong reasons. It is important to examine multiple related variables (e.g., different aerosol species, aerosol vertical profiles and

associated tracer concentrations) to ensure physically consistent simulations.

[6] In this study, we use multisatellite data combined with analysis and surface measurements to evaluate the performance of WRF-Chem in simulating deep convection and biomass burning over South America. This region has been identified with distinct signal of aerosol effects on clouds and precipitation [e.g., *Jiang et al.*, 2008; *Lin et al.*, 2006], while the performance of WRF-Chem in this tropical convective region has not been well documented, similarly for other regional models. We conduct a 9-day simulation at 36 km resolution. During these 9 days, enhanced AOT was observed over South America by the Moderate Resolution Imaging Spectroradiometer (MODIS) while increased CO accompanied with moderate deep convection were observed by the Microwave Limb Sounder (MLS) in the upper troposphere. The model evaluation will focus on the simulations of aerosol, chemistry, deep convective clouds and precipitation around the Amazon rain forest region. We aim to not only examine the performance of the WRF-Chem in simulating biomass burning and deep convection, but also to explore strategies for applications of satellite observations (especially from A-Train) in regional model development. We have also conducted a run with 4 km resolution but shorter duration (5 days). The comparison between the two experiments shows the sensitivity of model performance to horizontal resolutions. A companion paper (Part II: Biomass burning aerosol effects on clouds and precipitation) examines the biomass burning aerosol effects on clouds and precipitation over this region.

[7] The structure of the paper is as follows. In section 2, the model configuration and experiment design are presented. The data sets used for evaluations are described in section 3. In section 4, the simulated aerosol, chemical species, clouds and precipitation are compared to satellite observations and other available data sets. The strength and weakness in both model simulations and observations are identified. Section 5 includes conclusion and discussion.

2. Model Configuration

[8] The WRF-Chem Version 3.1.1 [*Grell et al.*, 2005] is used in this study. The control simulation runs at 36 km horizontal grid resolution, and with 28 eta levels in the vertical. The extent of the model domain for the control run is shown in the outer domain of Figure 1a. The microphysics scheme used in the simulations is the Lin et al. microphysics scheme [*Chen and Sun*, 2002] with a prognostic treatment of cloud droplet number [*Ghan et al.*, 1997] since it is the only one coupled to cloud-aerosol interactions in the WRF-Chem when we conducted this study. The Morrison scheme has been implemented for cloud-aerosol interactions and is now available to the public in the most recent release of WRF-Chem V3.3. Other primary physical schemes used in the simulations include the Rapid Radiative Transfer Model for Global climate models (RRTMG) longwave scheme [*Mlawer et al.*, 1997; *Iacono et al.*, 2000] and the Goddard [*Chou and Suarez*, 1994] shortwave scheme. The Grell-Devenyi ensemble cumulus scheme [*Grell and Dévényi*, 2002; *Grell et al.*, 1994] is used in the control simulation while no cumulus parameterization is employed in the sensitivity run.
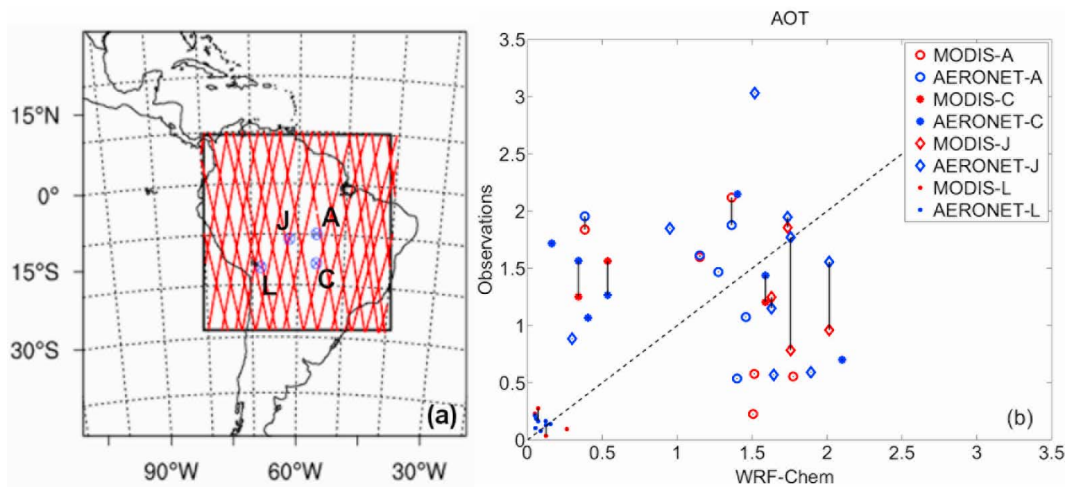
Figure 1. (a) Model domains used in this study: outer domain for the 36 km simulation, and inner domain for the 4 km simulation. Analysis is focused on the inner domain for both 36 km and 4 km simulations. The red lines are CloudSat/CALIPSO overpasses during the simulations from Sep. 16 to Sep. 23, 2006. Four AERONET stations are identified as A: Alta_Foresta; C: CUIABA-MIRANDA; J: Ji_Parana_SE; L: La_Paz. (b) Scatterplot of the daily averaged WRF-Chem AOT with the AERONET (blue) and MODIS (red) AOT measurements at 550 nm over four AERONET stations. Four AERONET stations are represented by different symbols. The observed AERONET and MODIS points on the same day are connected by black lines. The unsynchronized measurements are not connected.

The initial and boundary conditions for meteorology are obtained from the 1° × 1° National Center for Environmental Prediction final (NCEP FNL) Global Tropospheric Analyses (http://dss.ucar.edu/datasets/ds083.2/).

[9] The Regional Acid Deposition Model Version 2 (RADM2) [*Stockwell et al.*, 1990] is used as the chemistry driver, and the Modal Aerosol Dynamics Model for Europe (MADE/SORGAM) [*Ackermann et al.*, 1998; *Schell et al.*, 2001] is used as the aerosol driver. The anthropogenic emissions are provided by the 0.5° × 0.5° Reanalysis of the TROpospheric (RETRO) chemical composition over the past 40 years (http:/retro.enes.org/index.shtml) and the 1° × 1° Emission Database for Global Atmospheric Research (EDGAR) (http://www.mnp.nl/edgar/introduction). The initial and boundary conditions for chemical constituents and aerosols are obtained from the offline Model for Ozone and Related Chemical Tracers, version 4 (MOZART-4) global chemical transport model with a 2.8° × 2.8° horizontal resolution [*Emmons et al.*, 2010]. Comparing to Measurements Of Pollution In The Troposphere (MOPITT) and MODIS observations, the MOZART-4 model outputs show a high bias for the column-integrated CO over South America and a low bias for AOT in the nearby oceanic regions [*Emmons et al.*, 2010]. Since the species O_3 in the MOZART-4 is unrealistic in the stratosphere and upper troposphere [*Emmons et al.*, 2010], the species O3RAD (instead of O_3) in the MOZART-4 is used for the initial and boundary conditions of O_3 in the WRF-Chem simulations. The O3RAD variable is relaxed to the ozone climatology in the stratosphere and to the MOZART calculated ozone in the troposphere. It should be noticed that the O3RAD in the upper troposphere is much higher than observations due to too strong stratospheric flux from reanalysis meteorological data sets [*van Noije et al.*, 2004; *Emmons et al.*, 2010].

[10] Based on the fire locations from the geostationary NOAA weather satellite (GOES) fire data set WF_ABBA (www.nrlmry.navy.mil/flambe/index.html), emission rates of biomass burning tracers are estimated from the Brazilian Biomass Burning Emissions Model (3BEM), then the emitted tracers are injected into the atmosphere with a plume rise model [*Freitas et al.*, 2005; *Grell et al.*, 2011]. Black carbon (BC) and organic carbon (OC) are the two primary aerosol species emitted from biomass burning. Calculated from the 3BEM model, the surface emission rate of BC has an average of 2.62×10^{-3} mol km^{-2} h^{-1} with a maximum of 0.24 mol km^{-2} h^{-1} in the inner box of Figure 1a while the surface emission rate of OC has an average of 21.28×10^{-3} mol km^{-2} h^{-1} with a maximum of 3.86 mol km^{-2} h^{-1}. Large uncertainties on emission estimations can be contributed from estimations of fire size, emission factors, area and fuel burning processes, and plume rise processes [*Freitas et al.*, 2005; *Al-Saadi et al.*, 2008]. Compared with the MODIS AOT, the aerosol intensity calculated from the WF_ABBA fire data was much weaker than the observations although the spatial pattern agreed well with the observations from MODIS. Thus, we have increased the surface emission rates for BC and OC, which are calculated from the 3BEM model, by five times to match the MODIS AOT over the analysis area. Other aerosol species and trace gases from biomass burning are not altered. Additional physics and chemistry schemes used in this study are summarized in Table 1.

[11] The simulation initializes at 0000 UTC 15 September 2006 and runs for 9 days. Since the model is initialized with the FNL meteorology and MOZART-4 chemistry and aerosols, we treat the first 24 h of simulation as a spin-up. The modeled clouds and aerosols show approximately consistent diurnal variations after the first day (figure not shown).

Table 1. WRF-Chem V3.1.1 Physics and Chemistry Schemes Used for Both the 36 km and 4 km Simulations

Atmospheric Process	WRF-Chem Option
Microphysics	Purdue Lin et al. with a prognostic treatment of cloud droplet number
Cumulus	Grell-Devenyi ensemble in the 36 km simulation; No cumulus scheme in the 4 km simulation
Longwave radiation	RRTMG
Shortwave radiation	Goddard
Planetary boundary layer (PBL)	Mellor-Yamada-Janjic (Eta) TKE
Surface layer	Monin-Obukhov (Janjic)
Land surface	Unified Noah
Chemistry driver	RADM2
Aerosol driver	MADE/SORGAM
Anthropogenic emissions	RETRO and EDGAR
Biomass burning emissions	WF_ABBA fire locations, 3BEM and a plume rise model with modification on surface emission rate
Gas chemistry	On
Aerosol chemistry	On
Wet scavenging	On
Vertical turbulent mixing	On
Cloud chemistry	On
Aerosols-cloud-radiation interactions	On

Our analysis starts from 0000 UTC 16 September 2006 for an 8-day period. The analysis focuses on the inner domain in Figure 1a, where biomass burnings occurred. A sensitivity run at 4 km horizontal resolution is conducted with a smaller domain (the inner domain in Figure 1a) and a shorter time span (5 days).

3. Data Sets and Processing Method

3.1. Aura MLS Data Set

[12] The MLS on board Aura satellite measures microwave thermal emission from the limb of Earth's atmosphere. The MLS Level 2 products (V3.3) [*Livesey et al.*, 2011] of upper tropospheric CO, O_3, water vapor and IWC are used in this study to evaluate the model simulations in the upper troposphere. The MLS data at 215 hPa from Sep. 16 2006 to Sep. 24 2006 are averaged onto 8° (longitude) × 4° (latitude) grid boxes for horizontal maps. The horizontal and vertical resolutions and measurement uncertainties for each product are listed in Table 2. The MLS measurements are mostly independent products. For example, the uncertainty in temperature retrieval does not generally affect the water vapor retrieval [*Read et al.*, 2007]. Also, MLS measurements are generally not degraded by the presence of clouds and aerosols, whose particle sizes are typically much smaller than the measurement wavelengths. Very thick clouds (IWC > ~50 mg m^{-3}) can degrade the temperature and some species measurements [*Wu et al.*, 2008], but the retrieval algorithms [*Livesey et al.*, 2006] flag such measurements and they are not used here.

3.2. Aqua MODIS AOT

[13] The Aqua MODIS Level 2 aerosol product (MYD04) is used as a reference for our model experiments to reproduce the intensity of aerosols associated with biomass burning. We use the MODIS AOT at 550 nm product with 1° (latitude) × 1.5° (longitude) resolution. The AOT product has an estimated error of 0.05 over land and 0.03 over ocean [*Remer et al.*, 2005].

3.3. AERONET AOT

[14] The AERONET (AErosol RObotic NETwork) program is a ground-based remote-sensing aerosol network

providing continuous cloud-screened aerosol observations [*Holben et al.*, 1998]. Observations of four AERONET stations (shown in Figure 1) are used as independent data sets to evaluate the aerosol simulation in the WRF-Chem. The daily AOT at 675 nm and 440 nm are used to derive the 550 nm AOT with the Angström exponent. The uncertainty in the retrieval of AOT under cloud free conditions is about 0.01 [*Holben et al.*, 1998].

3.4. Aura TES CO and O_3

[15] The vertical distributions of tropospheric CO and O_3 are available from the Global Survey data of the Aura Tropospheric Emission Spectrometer (TES), which is a nadir and limb viewing infrared Fourier transform spectrometer [*Beer et al.*, 2001; *Beer*, 2006]. The Global Survey data only crossed the model inner domain in 3 days of the analysis period. The 3-day averaged vertical profiles from TES Level 2 CO and O_3 (V005) nadir data are compared against the vertical distributions of CO and O_3 in the WRF-Chem. Considering that the exact location and timing of model simulations may be shifted from observations, the model simulations within ±150 km of the TES overpasses are averaged and compared with the TES profiles. Taking into account the measurement sensitivity and vertical weighting function, the TES averaging kernels are applied to constrain the modeled vertical profiles for a fair comparison [*Luo et al.*, 2007a].

[16] The TES nadir O_3 product has high biases of 3–10 (5–15%) ppbv throughout troposphere [*Nassar et al.*, 2008; *Richards et al.*, 2008]. Over the tropics, the root mean square (RMS) measurement uncertainties of TES O_3 product in the troposphere are 16.3 ppbv below 500 hPa and 8.5 ppbv above

Table 2. The Basic Information for MLS V3.3 Products in the Upper Troposphere

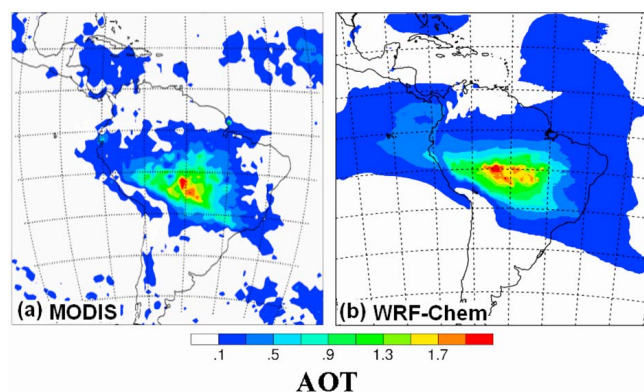| Product	Horizontal Resolution (km)	Vertical Resolution (km)	Measurement Uncertainty (%)
CO	700	5.5	30
O_3	400	3.0	5~20
Water vapor	240	2.7	8~25
IWC	300	4.0	100~300

Figure 2. The 8-day averaged AOT at 550 nm from Sep. 16 to Sep. 24, 2006. (a) MODIS; (b) WRF-Chem.

500 hPa [*Nassar et al.*, 2008]. For the TES CO, the RMS measurement uncertainty is typically within 15% [*Osterman et al.*, 2008; *Luo et al.*, 2007a, 2007b; *Lopez et al.*, 2008].

3.5. TRMM 3B42 Precipitation

[17] The Tropical Rainfall Measuring Mission (TRMM) 3B42 algorithm [*Huffman et al.*, 1995, 1997; *Huffman*, 1997] adjusts geostationary infrared (IR) precipitation estimates with an optimal combination of multimicrowave precipitation estimates, including TRMM Microwave Imager (TMI), Special Sensor Microwave/Imager (SSM/I), Advanced Microwave Scanning Radiometer (AMSR) and Advanced Microwave Sounding Unit (AMSU). Monthly rain gauge data are also used to rescale the 3B42 estimates. The TRMM 3B42 data set [*Huffman et al.*, 2001] provides 3-hourly gridded precipitation at a horizontal resolution of 0.25° × 0.25°. It is used in this study to validate the simulated precipitation in terms of spatial distribution and temporal evolution.

3.6. CALIPSO Aerosol Extinction and IWC

[18] CALIPSO provides the vertical structure of aerosol and clouds. The CALIPSO cloud (IWC) and the 532 nm aerosol extinction (AE) products (Version 3.01) with a horizontal resolution of 5 km [*Young and Vaughan*, 2009] are used to evaluate the vertical distribution of model simulated clouds and aerosol. Considering the CALIPSO data cannot retrieval cloud and aerosol simultaneously, the representation of cloud and aerosol in the CALIPSO data and the WRF-Chem simulations might be different in cloudy regions. Thus, the aerosol profiles are only calculated in clear sky conditions, for both CALIPSO and WRF-Chem. Similar averaging of model results around the satellite overpasses is performed as the TES data.

3.7. CloudSat Cloud Water Content (CWC)

[19] With a 94-GHz Cloud Profiling Radar (CPR), the CloudSat measures the backscattering by clouds from space. The vertical profiles of IWC and liquid water content (LWC) are retrieved from radar reflectivity (Ze) with empirical log linear relations between Ze and IWC/LWC [*Austin et al.*, 2009]. The CloudSat footprint is 1.7 km along track and 1.3 km cross track. As illustrated in Figure 1a, the overpasses of CloudSat data from Sep. 16 to Sep. 23 are sufficiently

sampled our analysis region. We average the model simulated CWC profiles within ±150 km of the CloudSat overpasses crossing the inner domain, similarly to the TES and CALIPSO data, when comparing to the CloudSat CWC.

3.8. Aqua AIRS Water Vapor

[20] The AIRS experiment on Aqua includes the Atmospheric Infrared Sounder (AIRS), the AMSU and the Humidity Sounder for Brazil (HSB). The AIRS Version 5 Level 3 daily gridded water vapor product (AIRX3STD) with 1° × 1° spatial resolution is used to evaluate the vertical distribution of water vapor in the WRF-Chem simulation. The water vapor products are retrieved from the combination of AIRS and AMSU observations because HSB has been ceased operating in February 2003. The AIRS water vapor product has RMS measurement uncertainties about ±25%, and biases of ∼10% at and below 200 hPa [*Fetzer et al.*, 2008] (also E. T. Olsen et al., AIRS/AMSU/HSB version 5 CalVal status summary, 2007, http://disc.sci.gsfc.nasa.gov/AIRS/documentation/v5_docs/v5_docs_list.shtml) (hereinafter Olsen et al., online summary, 2007).

3.9. NASA GEWEX SRB Data Set

[21] The Surface Radiation Budget (SRB) project is part of the National Aeronautics and Space Administration (NASA) Global Energy and Water cycle EXperiment (GEWEX). In the SRB data sets (http://www.gewex.org/srbdata.htm), the longwave algorithm used are adapted from the *Fu et al.* [1997] thermal infrared radiative transfer code while the shortwave algorithm are the *Pinker and Laszlo* [1992] short-wave algorithm. 3-hourly longwave and shortwave radiative fluxes at 1° × 1° horizontal resolution are produced using the input from the International Satellite Cloud Climatology Project (ISCCP) clouds and radiances, temperature and moisture from GEOS-4 (the 4-D data assimilation Goddard EOS Data Assimilation System, level-4) and other data sources. Validated with the ground-measured Baseline Surface Radiation Network (BSRN) data, the mean bias of longwave fluxes in the SRB data is 0.67 W m^{-2} and the RMS uncertainty is 30.2 W m^{-2}. For shortwave fluxes, the mean bias is −7.2 W m^{-2} while the RMS uncertainty is 87.7 W m^{-2}.

4. Model Evaluations

4.1. Aerosol

[22] The model domain is marked in Figure 1a, where extensive fires were observed from Sep. 15 to 24 over South America by GOES and MODIS satellites (not shown). Large amounts of aerosols are shown over the Amazonia basin in the MODIS AOT product, with a maximum AOT of 2.48 (Figure 2a). The WRF-Chem simulation (Figure 2b) with modified emission intensity produces similar aerosol pattern and comparable concentration to the MODIS AOT in the 8-day average.

[23] As an independent data source, the daily averaged AOT measurements from four AERONET stations inside the analysis domain are used to further evaluate the model simulations. MODIS observed and model simulated AOT are sampled to the four AERONET locations and scattered against the AERONET measurements in Figure 1b. It shows that the MODIS AOT generally in the same range with the AERONET data when both measurements are available. The
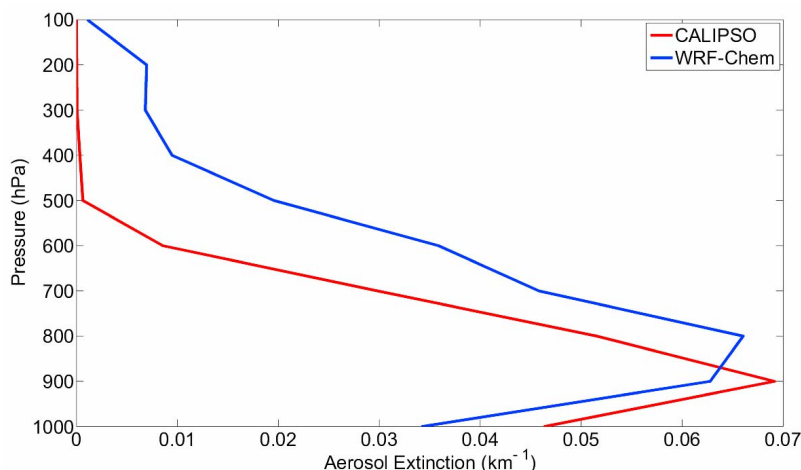
Figure 3. The 8-day averaged clear-sky aerosol extinction (km^{-1}) profiles at 532 nm: CALIPSO in red; WRF-Chem in blue. The WRF-Chem simulations are averaged within ±150 km of the CALIPSO overpasses across the inner analysis domain over the 8-day period.

model simulated AOT is within the range of individual satellite and surface observations, although it is not expected that the model simulated AOT matches perfectly with the point measurements since some individual fires may be missing in the model's boundary condition.

[24] CALIPSO AE profiles are used to evaluate the vertical distribution of clear-sky aerosols in the WRF-Chem simulation. As expected, more aerosols are distributed in the lower troposphere than in the upper atmospheric layers, in both the CALIPSO retrievals and the WRF-Chem simulations (Figure 3). CALIPSO AE shows a maximum of 0.069 at 900 hPa, and decreases sharply above 900 hPa. Above 500 hPa, the averaged aerosol extinction is very small because the occurrence frequency of aerosol decreases significantly with the increase of altitude. However, the instantaneous CALIPSO AE measurements at 200 hPa can be as high as 0.03. The aerosol profile in the WRF-Chem simulations roughly follows the distribution observed by CALIPSO, but with the AE maximum of 0.066 at 800 hPa. Comparing to the CALIPSO AE, the magnitude of AE in the WRF-Chem is smaller below 900 hPa but larger above 800 hPa. It shows that the vertical distribution of aerosols in the model may have large errors even though the vertical integrated AOT is close to the observation. This discrepancy may be a result of the deficiency in the plume rise model and/or misrepresented dynamical vertical transport of aerosols.

4.2. Chemistry

[25] As the distributions of CO and O_3 are strongly influenced by convection, we focus on these two chemical species to examine the convective mass transport in the model. Collocated with intensive aerosols over land, high CO loading in the upper troposphere is observed in the deep convective regions by MLS (Figure 4a). The simulated 8-day averaged CO at 215 hPa agrees with the MLS observation in both morphology and intensity (Figure 4b). The WRF-Chem simulated high CO shifts slightly counterclockwise from the observed counterpart, consistent with the shift of convective system as shown in other parameters discussed in later sections.

[26] The model simulated CO vertical profile shows that the peak CO occurs at lower troposphere near 825 hPa, corresponding to the highest AE (Figure 5a). CO decreases with height between 825 hPa and 400 hPa and shows a secondary broad local maximum around 200 hPa. The model simulated CO profile agrees with the MLS observation in the upper troposphere, considering the MLS data uncertainty. Since the MOZART-4 data are used in the WRF-Chem simulations as initial and boundary conditions, we show the MOZART data in Figure 5a to identify the difference between regional and climate models and the importance of initial and boundary conditions for regional models. It shows that the MOZART CO profile also exhibits two local maxima. However, the magnitude of MOZART CO is smaller than the WRF-Chem simulation in the lower troposphere. In the upper troposphere, the local maximum of MOZART CO shows at lower altitude comparing to the WRF-Chem CO, with a low bias comparing to MLS. It indicates that the convection in the MOZART might be not as strong as in the WRF-Chem. After application of the TES averaging kernels to the simulated profiles, the WRF-Chem modeled CO profile is within the uncertainty of the TES retrieval, with slightly weaker concentrations in the lower troposphere and higher values in the upper troposphere than the TES data.

[27] The MLS O_3 data at 215 hPa (Figure 4c) show low O_3 at low latitude and high values at higher latitude. A relatively low O_3 is seen near strong convective regions. The simulated O_3 (Figure 4d) roughly captures the distribution of O_3. The magnitude of the simulated upper tropospheric O_3 is larger than the MLS observations especially over the Amazonia basin where deep convection and biomass burning occur (see Figure 4b). The high bias in the modeled O_3 may result from the initial and boundary conditions from MOZART, which is relaxed to the climatology in the stratosphere. It may also indicate that the convection in the WRF-Chem is not strong enough to dilute the ozone in the upper troposphere.

[28] For the vertical distribution of O_3 (Figure 5b), the magnitude of the WRF-Chem O_3 shows good agreement with the MLS and TES data at 215 hPa. However, the WRF-Chem O_3 shows a sharper increase above 215 hPa with an order
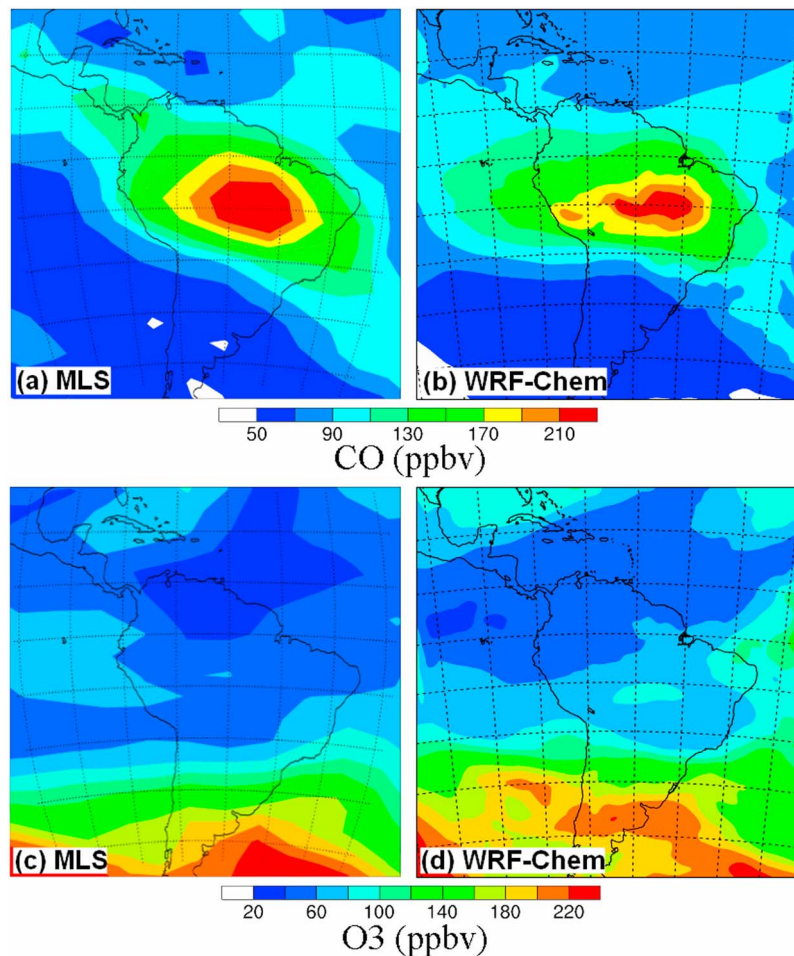
Figure 4. The distributions of the 8-day averaged chemical tracers (ppbv) at 215 hPa. (a) MLS CO; (b) WRF-Chem CO; (c) MLS O_3; (d) WRF-Chem O_3.

higher in magnitude than the MLS data. The sharp increase clearly follows the high biased MOZART upper tropospheric data [*van Noije et al.*, 2004; *Emmons et al.*, 2010], which serve as boundary conditions for our simulation. In order to limit the influence of much higher modeled stratospheric O_3 when applying the averaging kernels (AK) to the model simulation, the modeled O_3 profile above 215 is replaced by the TES a priori profile to extend each profile to the highest TES pressure level (0.1 hPa). Thus, our comparison between TES and model is limited to altitudes below 215 hPa. The AK-constrained model O_3 profile shows a low (high) bias below (above) 700 hPa, which may be related to the low (high) bias in the MOZART initial and boundary conditions. Previous studies have noted that the MOZART O_3 is generally biased low in the lower troposphere of the Southern Hemisphere [*Emmons et al.*, 2010]. The low O_3 bias below 700 hPa in the WRF-Chem is smaller than in the MOZART, suggesting an improvement in the regional model compared to the global model. Despite the biases in the modeled O_3, the simulation falls within the uncertainty range of the satellite observations, except above 215 hPa.

4.3. Surface Precipitation

[29] Shown from the TRMM 3B42 data set, a northwest-to-southeast (NW-SE) oriented precipitation band occurs across the South American continent (Figure 6a). Relatively heavy precipitation occurs over deep convective regions (northwest of South America) while moderate precipitation is observed over regions with intensive aerosols over the Amazonia basin. The other two NW-SE oriented precipitation bands take place over the ocean to the north and south of the continent. The WRF-Chem simulation (Figure 6b) approximately captures the distributions of the three precipitation bands. Over land, the magnitude of precipitation matches well with the observation although there is an eastward shift in the location of maximum precipitation. The magnitude and areal coverage of the simulated precipitation over ocean are larger than those in the TRMM observation. One reason for the large discrepancy over ocean may be due to the interference of lateral boundary condition as heavy precipitation over ocean is located near the boundary of the simulation domain. Since we are interested in the deep convective clouds and precipitation affected by biomass burning aerosols, the discrepancy over ocean is not the attention of this study.

[30] Figure 7 shows the time series of domain-averaged 3-h precipitation over land (the inner domain in Figure 1a). The intensity and temporal evolution of precipitation approximately agree well with the TRMM 3B42 data sets in this 36 km simulation. The 8-day averaged precipitation is
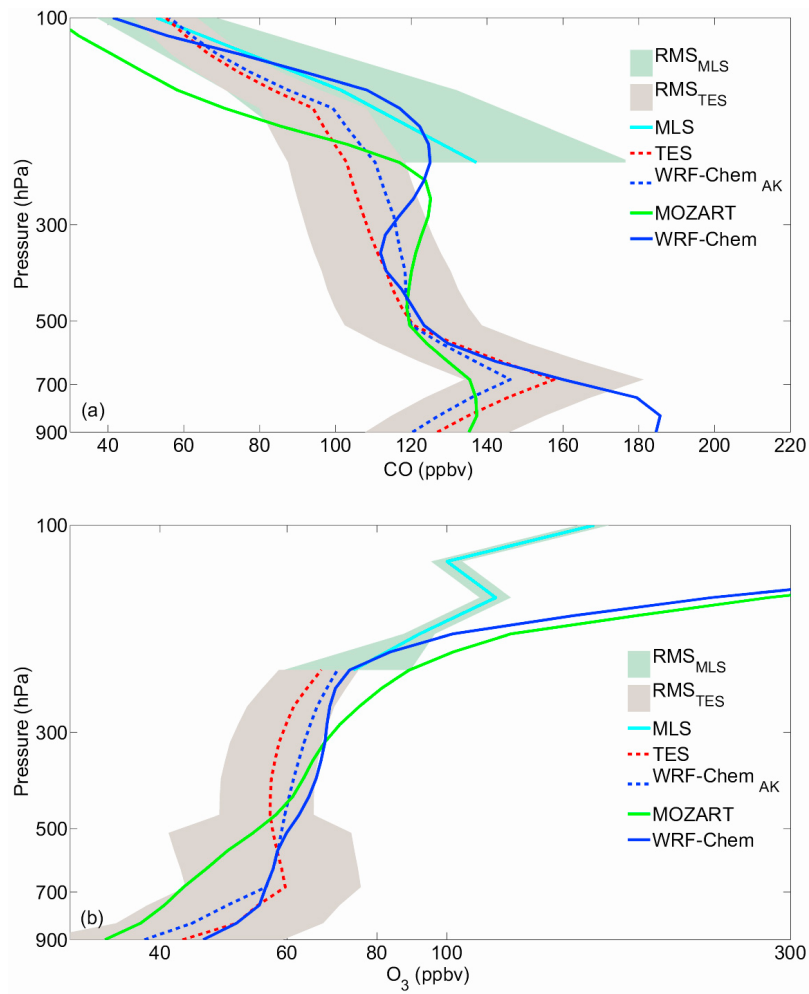
Figure 5. The 3-day averaged chemical tracer profiles (ppbv) over TES Global Survey overpasses. (a) CO; (b) O_3. The green lines are the original MOZART-4 data. The original WRF-Chem simulations are shown in solid blue lines. The constrained WRF-Chem simulations by the TES averaging kernels are shown in dashed blue lines. The dashed red lines are the TES observations. The MLS O_3 is shown in cyan. The shading areas represent the uncertainties for the TES and MLS data, respectively.
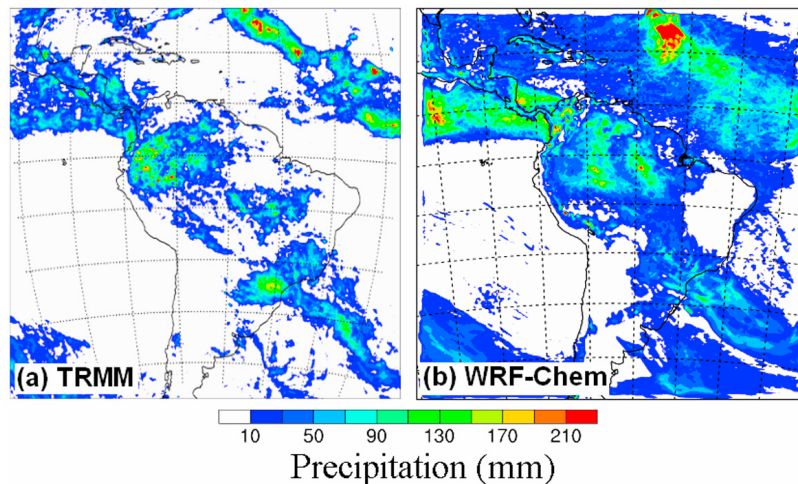

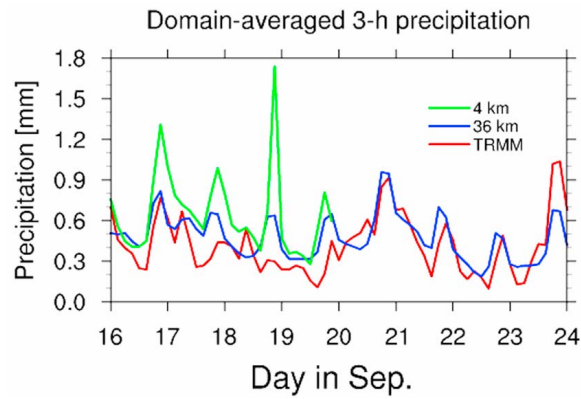**Figure 6.** The 8-day accumulated precipitation (mm). (a) TRMM 3B42; (b) WRF-Chem.

Figure 7. Time series of domain-averaged 3-h accumulated precipitation (mm), with the TRMM 3B42 data set in red; the 36 km simulation in blue and the 4 km simulation in green.

0.41 mm for TRMM and 0.48 mm in the 36-km simulation, about 17% higher than the observation. In the 36-km simulation, 89% of surface precipitation over land is produced from the cumulus scheme while 11% of surface precipitation is from the microphysical scheme.

4.4. Clouds and Water Vapor

[31] The 8-day averaged MLS IWC map at 215 hPa (Figure 8a) indicates deep convection occurred over the northwestern part of South America and extended into the central America, collocated with the intense precipitation over land. Another deep convective system was observed over the Atlantic Ocean at the northeastern corner of the model domain. The model simulation (Figure 8b) roughly reproduces the spatial distribution of upper tropospheric IWC. However, it significantly underestimates the magnitude of IWC by a factor of ~4 comparing with the MLS data, probably due to the use of cumulus parameterization in the 36 km simulation, limiting the amount of condensates on the grid scale.

[32] CloudSat, CALIPSO and MLS retrieved CWCs are used to evaluate the vertical distribution of equivalent water contents in the WRF-Chem simulation (Figure 9). Figure 9 also shows the averaged CloudSat CWC profile for non-precipitating scenes (the "CloudSat-NoRain" profile), which gives a lower bound of observed CWC profiles. The true CWC should lie in-between the CloudSat total and CloudSat-NoRain CWC profiles, although it is unclear exactly where the true value is. The measurement uncertainties for CloudSat and CALIPSO data are not available as the data validation
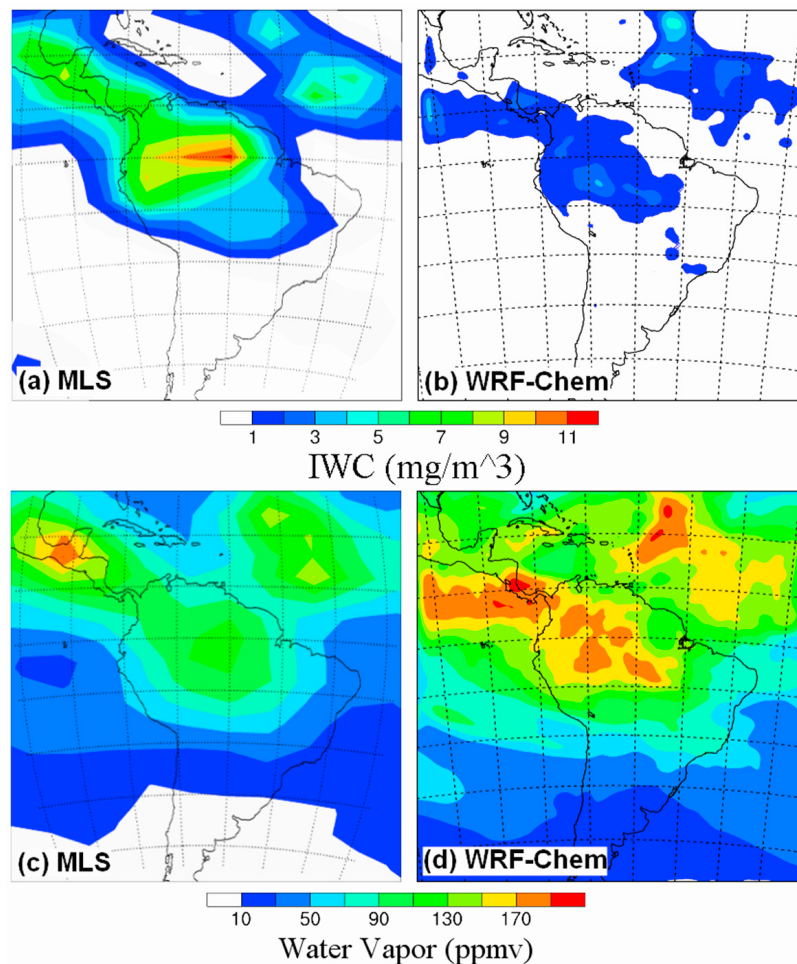

Figure 8. The 8-day averaged IWC (mg m^{-3}) and water vapor (ppmv) at 215 hPa. (a) MLS IWC; (b) WRF-Chem IWC; (c) MLS water vapor; (d) WRF-Chem water vapor.
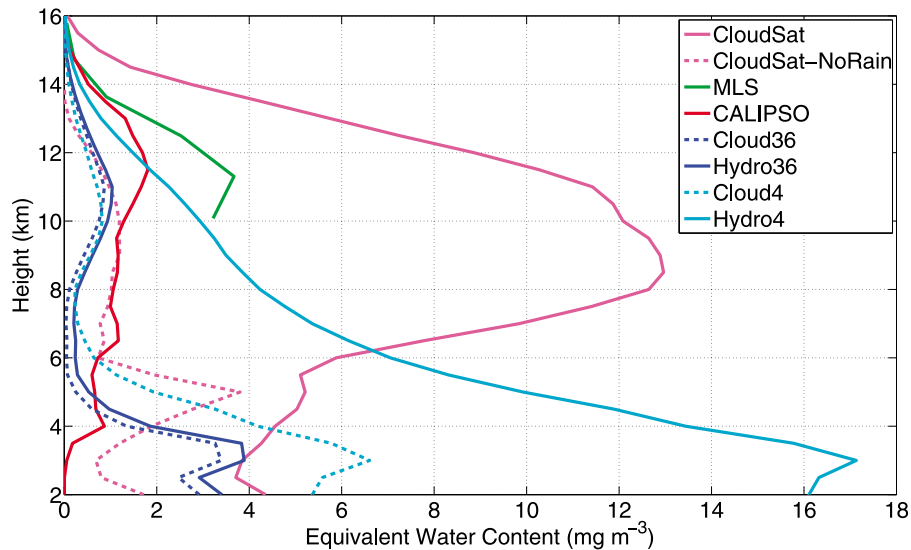
Figure 9. The vertical profiles of averaged equivalent water content (mg m^{-3}): CALIPSO LWC in red; CloudSat CWC in solid magenta line; CloudSat CWC excluding precipitating scenes in dashed magenta line; MLS in green; The dashed blue (cyan) line is the CWC profile including cloud water and cloud ice only in the 36 km (4 km) simulation; The solid blue (cyan) line is the CWC including clouds and precipitation particles in the 36 km (4 km) simulation. The data from the 4-km simulation are 4-day averages. The other data are 8-day averages, which are similar to their 4-day averages.

efforts are still ongoing. As CloudSat-retrieved CWC includes significant contribution of precipitating particles, we include rain, snow and graupel in the simulated total condensate profiles, indicated by "Hydro" in Figure 9, as opposed to "Cloud" for floating particles only.

[33] From the difference between the CloudSat and CloudSat-NoRain profiles (Figure 9), precipitation scenes contribute significantly to the averaged equivalent water content, especially for IWC. Large amounts of cloud water are associated with the deep convective system. MLS IWC is generally larger than the CALIPSO IWC because of the instrument sensitivies. Both MLS and CALIPSO IWC profiles fall within the CloudSat and CloudSat-NoRain CWC profiles above 10 km, confirming the fidelity of the observational data. Both MLS and CALIPSO IWC profiles show a local maximum at 11.5 km while the CloudSat CWC profile show a maximum of 12.96 mg m^{-3} at 8.5 km. The CALIPSO IWC profile is comparable with the CloudSat-NoRain profile in the middle layers between 6 km and 10 km but becomes smaller than the CloudSat-NoRain profile below 6 km, likely due to the inability of CALIPSO lidar to penetrate deep convective clouds.

[34] The modeled cloud and hydrometeor profiles are quite similar in the 36 km simulation because most of the precipitation is handled by the cumulus parameterization scheme and does not generate grid-scale hydrometers. On average, the equivalent water content of precipitating particles is about 13% of the total hydrometeors. Above 11 km and below 4 km, both modeled cloud and hydrometeor profiles fall within the CloudSat total and CloudSat-NoRain CWCs. However, the modeled cloud and hydrometeors are even smaller than the CloudSat-NoRain CWC between 4 km and 11 km. As mentioned in section 4.3, 89% of surface precipitation over land is of convective origin, produced from the cumulus parameterization scheme. In the cumulus scheme, all pre-

cipitating particles are converted to surface precipitation and no grid-scale hydrometeor is parameterized [*Grell et al.*, 1994]. Thus the total hydrometeor on the grid scale is significantly underestimated in the layer where precipitating particles account for a large portion of total condensates. The underestimate of cloud water in this layer also indicate the problem in the microphysical scheme although one should not expect the microphysics scheme to behave well at 36 km resolution with cumulus parameterization being active.

[35] High concentration of water vapor is observed by MLS at 215 hPa in deep convective regions (Figure 8c). The simulated water vapor at 215 hPa (Figure 8d) approximately captures the observed horizontal distribution, but with a high bias. Such high bias persists through 261 hPa to 147 hPa (Figure 10). AIRS show a dry bias in the upper troposphere relative to MLS due to the AIRS low-end threshold of 15–20 ppmv [*Fetzer et al.*, 2008; *Read et al.*, 2007]. The MLS data shows a less sharp decrease of water vapor above 147 hPa than the model simulation. Because the model top is set at 50 hPa, the lower water vapor in the model above 147 hPa may be affected by the upper boundary condition. Below 500 hPa, the simulated water vapor is within the uncertainty of the AIRS retrieval with slightly higher value than the AIRS data. Considering the 10% dry bias in the AIRS data [*Fetzer et al.*, 2008; Olsen et al., online summary, 2007], the model simulations shows good agreement with observations in the lower troposphere.

4.5. Radiative Fluxes

[36] To illustrate the model performance in radiation calculation, we choose to show a few commonly used parameters, including outgoing longwave radiation (OLR) at the top of atmosphere (TOA) and downward shortwave radiative flux at surface (SWDOWN). We use the 3-h averaged
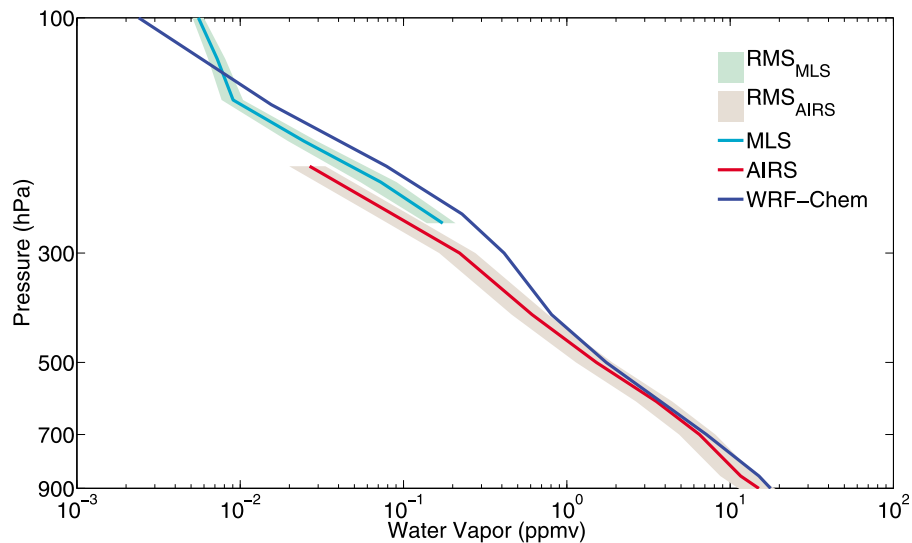
Figure 10. The vertical profiles of the 8-day averaged water vapor (ppmv) for AIRS (red), WRF-Chem (blue) and MLS (cyan). Shading areas are RMS measurement uncertainties for AIRS and MLS data, respectively.

radiative fluxes from the NASA GEWEX SRB data set for comparison.

[37] Throughout the 8-day simulation, the magnitude and temporal variation of OLR at TOA in the model agree well with the SRB data (Figure 11a). Since 1200 UTC 22 September, the SRB data set showed a significant decrease of OLR, which is not captured by the model simulation. On the average of the 8-day simulation, the model simulated OLR is 257 W m^{-2} while the SRB data set has an average of 251 W m^{-2}, suggesting fewer high clouds (or lower cloud top heights) are produced in the model.

[38] The simulated SWDOWN follows the temporal variation shown in the SRB data (Figure 11b). However, the magnitude of the modeled SWDOWN is larger than the SRB data, especially in the mid-day with largest difference shown in the afternoon on Sep 23, 2006. On average, the simulated SWDOWN is 248 W m^{-2} while it is 225 W m^{-2} in the SRB data set, consistent with the notion that the model produces fewer (or optically thinner) clouds than the observation. The difference between the model simulations and SRB data sets are within the measurement uncertainties of the SRB data sets.

4.6. Sensitivity to Model Resolution

[39] In order to test the sensitivity of simulated results to model resolution, a simulation at 4 km horizontal resolu-
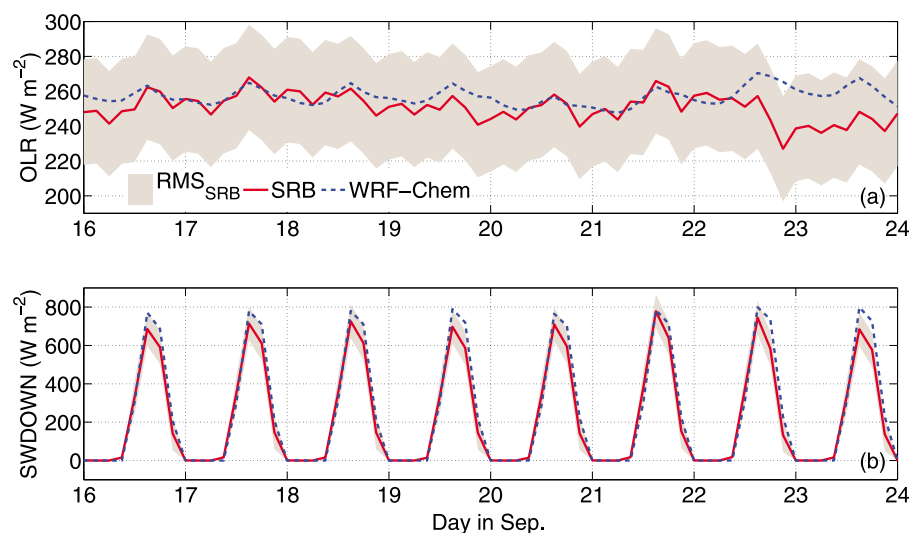

Figure 11. Time series of the WRF-Chem simulated radiative fluxes (dashed blue) compared with the SRB data (solid red), from 0000 UTC Sep. 16 to 0000 UTC Sep. 24, 2006. (a) Upward longwave radiative flux (OLR) (W m^{-2}) at the TOA; (b) Downward shortwave radiative flux (SWDOWN) at the surface (W m^{-2}). The shading areas are the RMS of the SRB data set.

tion is conducted with the cumulus scheme turned off. Clouds and precipitation are explicitly produced by the Lin et al. microphysics scheme. The 4-km simulation produces similar distribution and magnitude of aerosol and chemical tracers to the 36 km simulation (figures not shown). The 4 km simulation also reproduces the pattern (not shown) and evolution (Figure 7) of surface precipitation, but with a high bias, especially when precipitation is relatively high. The magnitude of clouds at 4 km is similar to the 36 km simulation while precipitating particles (mainly rainwater and graupel) have a large contribution to the total hydrometeor (Figure 9). The vertical distribution of hydrometeor at upper layers is within the bounds of the CloudSat and CloudSat-NoRain profiles, while the hydrometeor profile from the 4 km simulation is much closer to the MLS IWC in the upper troposphere than the profile from the 36 km simulation. However, the 4 km simulation shows a maximum of cloud and hydrometeor water content at 3 km. The magnitude of hydrometeor in the lower troposphere is much larger than the CloudSat retrieval. This high bias in the hydrometer profile is consistent with the high precipitation bias, likely a problem from the Lin et al. microphysics scheme. *Wu and Petty* [2010] found a similar high bias of precipitation with the Lin et al. microphysical scheme in the WRF simulation of polar lows, comparing to other four microphysical schemes.

5. Conclusion and Discussion

[40] This study employs multiple data sets to evaluate the performance of the WRF-Chem model in simulating deep convection and biomass burning during the dry season of South America. Multisatellite observations (mostly from the A-Train satellites), surface measurements and analysis data are used for comparison. In general, we find that the 36 km simulation approximately reproduces the horizontal and vertical distributions of aerosols, and chemical tracers in response to convection. The modeled precipitation agrees with the TRMM 3B42 data set, in both spatial distribution and temporal evolution. The patterns of upper tropospheric ice clouds and water vapor are approximately reproduced, although the magnitudes are different from the observations. The model simulations underestimate the magnitude of ice clouds while they overestimate the magnitude of water vapor in the upper troposphere, an indication of deficiency in the current choice of model setup. The model simulation captures the temporal variation and magnitude of the SWDOWN and OLR at TOA with biases pointing to an underestimate of cloud amount and cloud top heights, especially in the last 36 h of the simulation.

[41] The magnitude of total hydrometeors in the upper troposphere and mid-troposphere are significantly lower than satellite observations in the 36 km run, partly because the cumulus parameterization does not produce grid-scale hydrometeor profiles. However, between 4 km and 11 km, the cloud and hydrometeor amount in the model is even lower than the CloudSat-NoRain CWC, suggesting that the microphysical scheme significantly underestimates cloud water content when cumulus parameterization scheme is active.

[42] The 4 km simulation overestimates the surface precipitation, rainwater and graupel. Although the finer horizontal resolution is desirable to better resolve convection,

it does not necessarily produce superior hydrological cycle because of the heavy dependency of hydrological parameters on the microphysical scheme. The overestimation of precipitation and clouds by the Lin et al. microphysical scheme has been found by previous studies [e.g., *Wu and Petty*, 2010]. Efforts are certainly needed to improve the microphysical scheme in the WRF-Chem for accurate assessment of the aerosol effects on regional and global climate.

[43] Besides the problem with the model's microphysical scheme, we find two other factors important for accurate chemical weather simulations. One is the emission data and the other is the initial and boundary conditions for chemistry. For the aerosol simulation, emission data are of critically importance. We have manually modified the surface emission intensity to match the MODIS observed AOT during the simulation time period. A vigorous updating of emission inventory is needed for accurate simulation of pollution episodes in various regions, although it is not an easy task. The model simulated CO and O_3 vertical profiles are largely influenced by the MOZART initial and boundary conditions. Improvements on the initial and boundary condition for chemistry are certainly needed in the WRF-Chem.

[44] Different from many regional modeling studies that used field campaign and in situ measurements to evaluate model performance, our study innovatively employs a suite of satellite measurements. These satellite measurements provide independent and complementary information on the coupled meteorological, chemical and radiative processes. Therefore, the multiangle comprehensive examination of model simulations reveals better the consistency in the model physics than using a single measurement. Moreover, satellite measurements have unique spatial and temporal coverage and retrieval limitations. Our analysis explores the strategies for proper use of these measurements, including application of vertical averaging kernels and horizontal averaging to match data and model simulations on large-scales. The uncertainties of satellite measurements are also clearly specified when comparing with model results. Hence, this model-data comparison study can serve as a useful example for future usage of satellite observations for regional modeling studies. The satellite data sets that we have explored can be combined with field campaign and in situ measurements to help regional model evaluation and data assimilation for improved predictions of regional weather and climate.

[45] Overall, the WRF-Chem model with fully coupled meteorology-aerosol-chemistry provides a valuable tool to investigate the interactions among aerosol, clouds, precipitation and chemical tracers. The reasonable performance of 36 km and 4 km simulations enable us to conduct a series of sensitivity experiments to examine the roles of aerosols in changing clouds and precipitation. The impact of biomass burning aerosols on clouds and precipitation are shown in the companion paper [*Wu et al.*, 2011] (Biomass burning aerosol effects on clouds and precipitation).

References

Ackermann, I. J., H. Hass, M. Memmesheimer, A. Ebel, F. S. Binkowski, and U. Shankar (1998), Modal aerosol dynamics model for Europe: Development and first applications, *Atmos. Environ.*, *32*(17), 2981–2999, doi:10.1016/S1352-2310(98)00006-5.

Al-Saadi, J., et al. (2008), Intercomparison of near-real-time biomass burning emissions estimates constrained by satellite fire data, *J. Appl. Remote Sens.*, *2*, 021504, doi:10.1117/1.2948785.

Andreae, M. O., et al. (2001), Transport of biomass burning smoke to the upper troposphere by deep convection in the equatorial region, *Geophys. Res. Lett.*, *28*(6), 951–954, doi:10.1029/2000GL012391.

Andreae, M. O., D. Rosenfeld, P. Artaxo, A. A. Costa, G. P. Frank, K. M. Longo, and M. A. F. Silva-Dias (2004), Smoking rain clouds over the Amazon, *Science*, *303*, 1337–1342, doi:10.1126/science.1092779.

Austin, R. T., A. J. Heymsfield, and G. L. Stephens (2009), Retrieval of ice cloud microphysical parameters using the CloudSat millimeter-wave radar and temperature, *J. Geophys. Res.*, *114*, D00A23, doi:10.1029/2008JD010049.

Barnard, J. C., J. D. Fast, G. Paredes-Miranda, W. P. Arnott, and A. Laskin (2010), Technical Note: Evaluation of the WRF-Chem "Aerosol Chemical to Aerosol Optical Properties" Module using data from the MILAGRO campaign, *Atmos. Chem. Phys.*, *10*, 7325–7340, doi:10.5194/acp-10-7325-2010.

Beer, R. (2006), TES on the Aura mission: Scientific objectives, measurements, and analysis overview, *IEEE Trans. Geosci. Remote Sens.*, *44*, 1102–1105, doi:10.1109/TGRS.2005.863716.

Beer, R., T. A. Glavich, and D. M. Rider (2001), Tropospheric Emission Spectrometer for the Earth Observing System Aura satellite, *Appl. Opt.*, *40*, 2356–2367, doi:10.1364/AO.40.002356.

Chapman, E. G., W. I. Gustafson Jr., R. C. Easter, J. C. Barnard, S. J. Ghan, M. S. Pekour, and J. D. Fast (2009), Coupling aerosol-cloud-radiative processes in the WRF-Chem model: Investigating the radiative impact of elevated point sources, *Atmos. Chem. Phys.*, *9*, 945–964, doi:10.5194/acp-9-945-2009.

Chen, S.-H., and W.-Y. Sun (2002), A one-dimensional time dependent cloud model, *J. Meteorol. Soc. Jpn.*, *80*, 99–118, doi:10.2151/jmsj.80.99.

Chou, M.-D., and M. J. Suarez (1994), An efficient thermal infrared radiation parameterization for use in general circulation models, *NASA Tech. Memo., TM-104606*, vol. 3, 85 pp., NASA Goddard Space Flight Cent., Greenbelt, Md.

Emmons, L. K., et al. (2010), Description and evaluation of the Model for Ozone and Related chemical Tracers, version 4(MOZART-4), *Geosci. Model Dev.*, *3*, 43–67, doi:10.5194/gmd-3-43-2010.

Fast, J., et al. (2009), Evaluating simulated primary anthropogenic and biomass burning organic aerosols during MILAGRO: Implications for assessing treatments of secondary organic aerosols, *Atmos. Chem. Phys.*, *9*, 6191–6215, doi:10.5194/acp-9-6191-2009.

Fetzer, E. J., et al. (2008), Comparison of upper tropospheric water vapor observations from the Microwave Limb Sounder and Atmospheric Infrared Sounder, *J. Geophys. Res.*, *113*, D22110, doi:10.1029/2008JD010000.

Folkins, I., R. Chatfield, D. Baumgardner, and M. Proffitt (1997), Biomass burning and deep convection in southeastern Asia: Results from ASHOE/MAESA, *J. Geophys. Res.*, *102*(D11), 13,291–13,299, doi:10.1029/96JD03711.

Freitas, S. R., K. M. Longo, M. Silva Dias, P. Silva Dias, R. Chatfield, E. Prins, P. Artaxo, G. Grell, and F. Recuero (2005), Monitoring the transport of biomass burning emissions in South America, *Environ. Fluid Mech.*, *5*(1–2), 135–167, doi:10.1007/s10652-005-0243-7.

Fu, Q., K. N. Liou, M. C. Cribb, T. P. Charlock, and A. Grossman (1997), Multiple scattering parameterization in thermal infrared radiative transfer, *J. Atmos. Sci.*, *54*, 2799–2812, doi:10.1175/1520-0469(1997)054<2799:MSPITI>2.0.CO;2.

Ghan, S. J., L. R. Leung, R. C. Easter, and H. Abdul-Razzak (1997), Prediction of cloud droplet number in a general circulation model, *J. Geophys. Res.*, *102*(D18), 21,777–21,794, doi:10.1029/97JD01810.

Grell, G. A., and D. Dévényi (2002), A generalized approach to parameterizing convection combining ensemble and data assimilation techniques, *Geophys. Res. Lett.*, *29*(14), 1693, doi:10.1029/2002GL015311.

Grell, G. A., J. Dudhia, and D. R. Stauffer (1994), A description of the Fifth generation Penn State/NCAR Mesoscale Model (MM5), *NCAR Tech Note TN-398 + STR*, 122 pp., Natl. Cent. for Atmos. Res., Boulder, Colo.

Grell, G. A., S. E. Peckham, R. Schmitz, S. A. McKeen, G. Frost, W. C. Skamarock, and B. Eder (2005), Fully coupled "online" chemistry within the WRF model, *Atmos. Environ.*, *39*, 6957–6975, doi:10.1016/j.atmosenv.2005.04.027.

Grell, G., S. R. Freitas, M. Stuefer, and J. Fast (2011), Inclusion of biomass burning in WRF-Chem: Impact of wildfires on weather forecasts, *Atmos. Chem. Phys.*, *11*, 5829–5303, doi:10.5194/acp-11-5289-2010.

Gustafson, W. I., Jr., E. G. Chapman, S. J. Ghan, R. C. Easter, and J. D. Fast (2007), Impact on modeled cloud characteristics due to simplified treatment of uniform cloud condensation nuclei during NEAQS 2004, *Geophys. Res. Lett.*, *34*, L19809, doi:10.1029/2007GL030021.

Hegarty, J., H. Mao, and R. Talbot (2010), Winter- and summertime continental influences on tropospheric O_3 and CO observed by TES over the western North Atlantic Ocean, *Atmos. Chem. Phys.*, *10*, doi:10.5194/acp-10-3723-2010.

Holben, B. N., et al. (1998), AERONET—A federated instrument network and data archive for aerosol characterization, *Remote Sens. Environ.*, *66*, 1–16, doi:10.1016/S0034-4257(98)00031-5.

Huffman, G. J. (1997), Estimates of root-mean-square random error for finite samples of estimated precipitation, *J. Appl. Meteorol.*, *36*, 1191–1201, doi:10.1175/1520-0450(1997)036<1191:EORMSR>2.0.CO;2.

Huffman, G. J., R. F. Adler, B. Rudolf, U. Schneider, and P. R. Keehn (1995), Global precipitation estimates based on a technique for combining satellite-based estimates, rain gauge analysis, and NWP model precipitation information, *J. Clim.*, *8*, 1284–1295, doi:10.1175/1520-0442(1995)008<1284:GPEBOA>2.0.CO;2.

Huffman, G. J., R. F. Adler, P. Arkin, A. Chang, R. Ferraro, A. Gruber, J. Janowiak, A. McNab, B. Rudolph, and U. Schneider (1997), The global precipitation climatology project (GPCP) combined precipitation dataset, *Bull. Am. Meteorol. Soc.*, *78*, 5–20, doi:10.1175/1520-0477(1997)078<0005:TGPCPG>2.0.CO;2.

Huffman, G. J., R. F. Adler, M. Morrissey, D. T. Bolvin, S. Curtis, R. Joyce, B. McGavock, and J. Susskind (2001), Global precipitation at one-degree daily resolution from multisatellite observations, *J, Hydrometeorol.*, *2*, 36–50, doi:10.1175/1525-7541(2001)002<0036:GPAODD>2.0.CO;2.

Iacono, M. J., E. J. Mlawer, S. A. Clough, and J.-J. Morcrette (2000), Impact of an improved longwave radiation model, RRTM, on the energy budget and thermodynamic properties of the NCAR community climate model, CCM3, *J. Geophys. Res.*, *105*(D11), 14,873–14,890, doi:10.1029/2000JD900091.

Jiang, J. H., H. Su, M. R. Schoeberl, S. T. Massie, P. Colarco, S. Platnick, and N. J. Livesey (2008), Clean and polluted clouds: Relationships among pollution, ice clouds, and precipitation in South America, *Geophys. Res. Lett.*, *35*, L14804, doi:10.1029/2008GL034631.

L'Ecuyer, T. S., and J. H. Jiang (2010), Touring the atmosphere aboard the A-Train, *Phys. Today*, *63*(7), 36–41, doi:10.1063/1.3463626.

Lin, J. C., T. Matsui, R. A. Pielke Sr., and C. Kummerow (2006), Effects of biomass-burning-derived aerosols on precipitation and clouds in the Amazon Basin: A satellite-based empirical study, *J. Geophys. Res.*, *111*, D19204, doi:10.1029/2005JD006884.

Lin, M., T. Holloway, G. R. Carmichael, and A. M. Fiore (2010), Quantifying pollution inflow and outflow over East Asia in spring with regional and global models, *Atmos. Chem. Phys.*, *10*, 4221–4239, doi:10.5194/acp-10-4221-2010.

Liu, J., J. A. Logan, D. B. A. Jones, N. J. Livesey, I. Megretskaia, C. Carouge, and P. Nedelec (2010), Analysis of CO in the tropical troposphere using Aura satellite data and the GEOS-Chem model: Insights into transport characteristics of the GEOS meteorological products, *Atmos. Chem. Phys.*, *10*, 12,207–12,232, doi:10.5194/acp-10-12207-2010.

Livesey, N. J., W. V. Snyder, W. G. Read, and P. A. Wagner (2006), Retrieval algorithms for the EOS Microwave Limb Sounder (MLS) instrument, *IEEE Trans. Geosci. Remote Sens.*, *44*(5), 1144–1155, doi:10.1109/TGRS.2006.872327.

Livesey, N. J., et al. (2011), EOS Aura Microwave Limb Sounder Version 3.3 Level 2 data quality and description document, *JPL Doc. D-33509*, Jet Propul. Lab., Pasadena, Calif.

Lopez, J. P., M. Luo, L. E. Christensen, M. Loewenstein, H. Jost, C. R. Webster, and G. Osterman (2008), TES carbon monoxide validation during two AVE campaigns using the Argus and ALIAS instruments on NASA's WB-57F, *J. Geophys. Res.*, *113*, D16S47, doi:10.1029/2007JD008811.

Luo, M., et al. (2007a), Comparison of carbon monoxide measurements by TES and MOPITT: Influence of a priori data and instrument characteris-

tics on nadir atmospheric species retrievals, *J. Geophys. Res.*, *112*, D09303, doi:10.1029/2006JD007663.

Luo, M., et al. (2007b), TES carbon monoxide validation with DACOM aircraft measurements during INTEX-B 2006, *J. Geophys. Res.*, *112*, D24S48, doi:10.1029/2007JD008803.

Martins, J. A., M. A. F. Silva Dias, and F. L. T. Gonçalves (2009), Impact of biomass burning aerosols on precipitation in the Amazon: A modeling case study, *J. Geophys. Res.*, *114*, D02207, doi:10.1029/2007JD009587.

Mlawer, E. J., S. J. Taubman, P. D. Brown, M. J. Iacono, and S. A. Clough (1997), Radiative transfer for inhomogeneous atmosphere: RRTM, a validated correlated-k model for the longwave, *J. Geophys. Res.*, *102*(D14), 16,663–16,682, doi:10.1029/97JD00237.

Nassar, R., et al. (2008), Validation of Tropospheric Emission Spectrometer (TES) nadir ozone profiles using ozonesonde measurements, *J. Geophys. Res.*, *113*, D15S17, doi:10.1029/2007JD008819.

Ntelekos, A. A., J. A. Smith, L. Donner, J. D. Fast, W. I. Gustafson, E. G. Chapman, and W. F. Krajewski (2009), The effects of aerosols on intense convective precipitation in the northeastern United States, *Q. J. R. Meteorol. Soc.*, *135*, 1367–1391, doi:10.1002/qj.476.

Osterman, G., et al. (2008), Validation of Tropospheric Emission Spectrometer (TES) measurements of the total, stratospheric and tropospheric column abundance of ozone, *J. Geophys. Res.*, *113*, D15S16, doi:10.1029/2007JD008801.

Pinker, R. T., and I. Laszlo (1992), Modeling of surface solar irradiance for satellite applications on a global scale, *J. Appl. Meteorol.*, *31*, 194–211, doi:10.1175/1520-0450(1992)031<0194:MSSIFS>2.0.CO;2.

Read, W. G., et al. (2007), Aura Microwave Limb Sounder upper tropospheric and lower stratospheric H_2O and relative humidity with respect to ice validation, *J. Geophys. Res.*, *112*, D24S35, doi:10.1029/2007JD008752.

Remer, L. A., et al. (2005), The MODIS aerosol algorithm, products, and validation, *J. Atmos. Sci.*, *62*, 947–973, doi:10.1175/JAS3385.1.

Richards, N. A. D., G. B. Osterman, E. V. Browell, J. W. Hair, M. Avery, and Q. Li (2008), Validation of Tropospheric Emission Spectrometer ozone profiles with aircraft observations during the Intercontinental Chemical Transport Experiment–B, *J. Geophys. Res.*, *113*, D16S29, doi:10.1029/2007JD008815.

Schell, B., I. J. Ackermann, H. Hass, F. S. Binkowski, and A. Ebel (2001), Modeling the formation of secondary organic aerosol within a comprehensive air quality model system, *J. Geophys. Res.*, *106*(D22), 28,275–28,293, doi:10.1029/2001JD000384.

Stockwell, W. R., P. Middleton, J. S. Chang, and X. Tang (1990), The second generation regional acid deposition model chemical mechanism for regional air quality modeling, *J. Geophys. Res.*, *95*(D10), 16,343–16,367, doi:10.1029/JD095iD10p16343.

Tie, X., S. Madronich, G. Li, Z. Ying, A. Weinheimer, E. Apel, and T. Campos (2009), Simulation of Mexico City plumes during the MIRAGE-Mex field campaign using the WRF-Chem model, *Atmos. Chem. Phys.*, *9*, 4621–4638, doi:10.5194/acp-9-4621-2009.

van Noije, T. P. C., H. J. Eskes, M. van Weele, and P. F. J. van Velthoven (2004), Implications of the enhanced Brewer-Dobson circulation in European Centre for Medium-Range Weather Forecasts reanalysis ERA-40 for the stratosphere-troposphere exchange of ozone in global chemistry transport models, *J. Geophys. Res.*, *109*, D19308, doi:10.1029/2004JD004586.

Wu, D. L., J. H. Jiang, W. G. Read, R. T. Austin, C. P. Davis, A. Lambert, G. L. Stephens, D. G. Vane, and J. W. Waters (2008), Validation of the Aura MLS Cloud Ice Water Content (IWC) Measurements, *J. Geophys. Res.*, *113*, D15S10, doi:10.1029/2007JD008931.

Wu, L., and G. W. Petty (2010), Intercomparison of bulk microphysics schemes in model simulations of polar lows, *Mon. Weather Rev.*, *138*, 2211–2228, doi:10.1175/2010MWR3122.1.

Wu, L., H. Su, and J. H. Jiang (2011), Regional simulations of deep convection and biomass burning over South America: 2. Biomass burning aerosol effects on clouds and precipitation, *J. Geophys. Res.*, doi:10.1029/2011JD016106, in press.

Young, S. A., and M. A. Vaughan (2009), The retrieval of profiles of particulate extinction from Cloud-Aerosol Lidar Infrared Pathfinder Satellite Observations (CALIPSO) data: Algorithm description, *J. Atmos. Oceanic Technol.*, *26*, 1105–1119, doi:10.1175/2008JTECHA1221.1.

Zhang, Y., R. Fu, H. Yu, R. E. Dickinson, R. N. Juarez, M. Chin, and H. Wang (2008), A regional climate model study of how biomass burning aerosol impacts land-atmosphere interactions over the Amazon, *J. Geophys. Res.*, *113*, D14S15, doi:10.1029/2007JD009449.

Zhang, Y., R. Fu, H. Yu, Y. Qian, R. Dickinson, M. A. F. Silva Dias, P. L. da Silva Dias, and K. Fernandes (2009), Impact of biomass burning aerosol on the monsoon circulation transition over Amazonia, *Geophys. Res. Lett.*, *36*, L10814, doi:10.1029/2009GL037180.

Zhao, C., X. Liu, L. R. Leung, B. Johnson, S. A. McFarlane, W. I. Gustafson Jr., J. D. Fast, and R. Easter (2010), The spatial distribution of mineral dust and its shortwave radiative forcing over North Africa: Modeling sensitivities to dust emissions and aerosol size treatments, *Atmos. Chem. Phys.*, *10*, 8821–8838, doi:10.5194/acp-10-8821-2010.

J. H. Jiang, H. Su, and L. Wu, Aura Microwave Limb Sounder (MLS) Science Team, Jet Propulsion Laboratory, California Institute of Technology, 4800 Oak Grove Dr., M/S 183-701, Pasadena, CA 91109, USA. (longtao.wu@jpl.nasa.gov)